CRYSTAL GROWTH & DESIGN

pubs.acs.org/crystal

Article

Mn^{2+}-Induced Robust Radiation Hardness in $Bi_4Ge_3O_{12}$ for Next-Generation High-Energy Physical Colliders

Mingxue Deng,* Lei Chen, Xiang Li, Xuejun Qi, Shaohan Wang, and Junfeng Chen*

Cite This: *Cryst. Growth Des.* 2025, 25, 1477−1483

Read Online

ACCESS | Metrics & More | Article Recommendations | Supporting Information

ABSTRACT: Future high-performance particle colliders, e.g., the proposed circular electron positron collider (CEPC) or future circular collider (FCC), demand unprecedented levels of accuracy in energy measurement for calorimeters. Although the proposed high-granularity crystal electromagnetic calorimeter has made great progress in recent years, the designing and matching of $Bi_4Ge_3O_{12}$ (BGO) scintillators with lower light output and higher radiation resistance, as well as not introducing slow components, lag far behind. Here, a Mn-doped BGO powder exhibits robust radiation resistance with a faster decay time, accelerating by 15%. Doping with Mn3% reduces the intensities of photoluminescence (PL) and radioluminescence (RL) to 55% and 22%, respectively, of those observed in pure BGO powder. Furthermore, Mn-doped BGO exhibits enhanced radiation resistance and can maintain 72% of the initial RL intensity within 2 h of radiation with a high-power UV lamp, while that of pure BGO is severely degraded to 45%. Theoretical calculation mechanism studies show that Mn doping not only maintains the intrinsic luminescence of BGO but also introduces a new intermediate energy level in the energy band to inhibit the formation of color centers. This work provides a new avenue to search for or discover scintillators from existing cost-effective scintillators for future high-energy physics experiments.

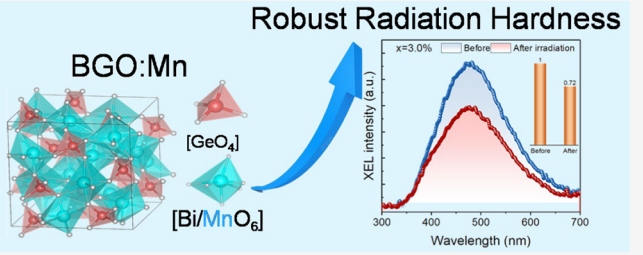

1. INTRODUCTION

After the discovery of the Higgs particle in 2012, the current period is considered to be the best window to explore potential new physics related to the Higgs boson. The international field of high-energy physics has proposed the future lepton collider experiments, such as the circular electron positron collider (CEPC) and the future circular collider (FCC).[1−3] They belong to intensity and energy frontier experimental facilities, which require several hundred tons of high-density inorganic scintillation crystals with robust radiation resistance and fast decay to meet the challenges of unprecedented high energy and counting rates.[4] A high-granularity crystal electromagnetic calorimeter (ECAL) is an attractive novel design with high-granularity crystal and silicon photomultiplier (SiPM) to achieve optimal electromagnetic energy resolution.[5] However, the limited dynamic range of SiPM and the large number of scintillation photons produced by GeV−TeV energetic particles will yield a saturation effect in SiPM devices.[6] Thus, it is vital to reduce the light output and improve the radiation resistance of the scintillator.

A bismuth germanate ($Bi_4Ge_3O_{12}$, BGO) crystal, as a promising scintillator candidate for crystal ECALs in CEPC and FCC facilities, has excellent comprehensive performance, such as high stopping power, good uniformity, stable physical and chemical properties, etc.[7] The BGO crystal, as a cost-effective scintillator with high density, is widely used in the fields of HEP, nuclear physics, astrophysics, medical imaging, resource exploration, etc.[8] In order to meet the application needs of future large HEP scientific facilities such as CEPC and FCC, it is urgent to develop BGO crystals with lower light output and robust radiation resistance, as well as no slow components.

Element doping is an effective approach for modulating the properties of scintillating materials. Spurrier et al. found that Ca−Ce codoping can shorten the decay time of lutetium silicate crystals to ∼30 ns and enhance their light output.[9] Chen et al. found that Y doping can effectively inhibit the slow component of BaF_2 crystals while maintaining its subnanosecond fast component, and that large-size high-quality doped crystals are feasible.[10,11] Li et al. improved the radioluminescence (RL) efficiency of $Cs_3Cu_2I_5$ crystals by doping Mn^{2+}.[12] In terms of doping modification of BGO crystals, Wei et al. found that Eu doping improves the radiation resistance of BGO but results in afterglow.[13,14] Okazaki et al. reported that the doping of Er^{3+} ions produces a new near-infrared light emission.[15] Dunaeva investigated that Dy^{3+}-doped BGO crystals have a fluorescence lifetime of 630 μs.[16] Deng et al. reported the enhancement of the optical output of BGO by a

Received: November 17, 2024
Revised: January 16, 2025
Accepted: January 17, 2025
Published: February 10, 2025

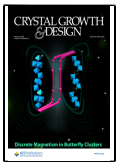

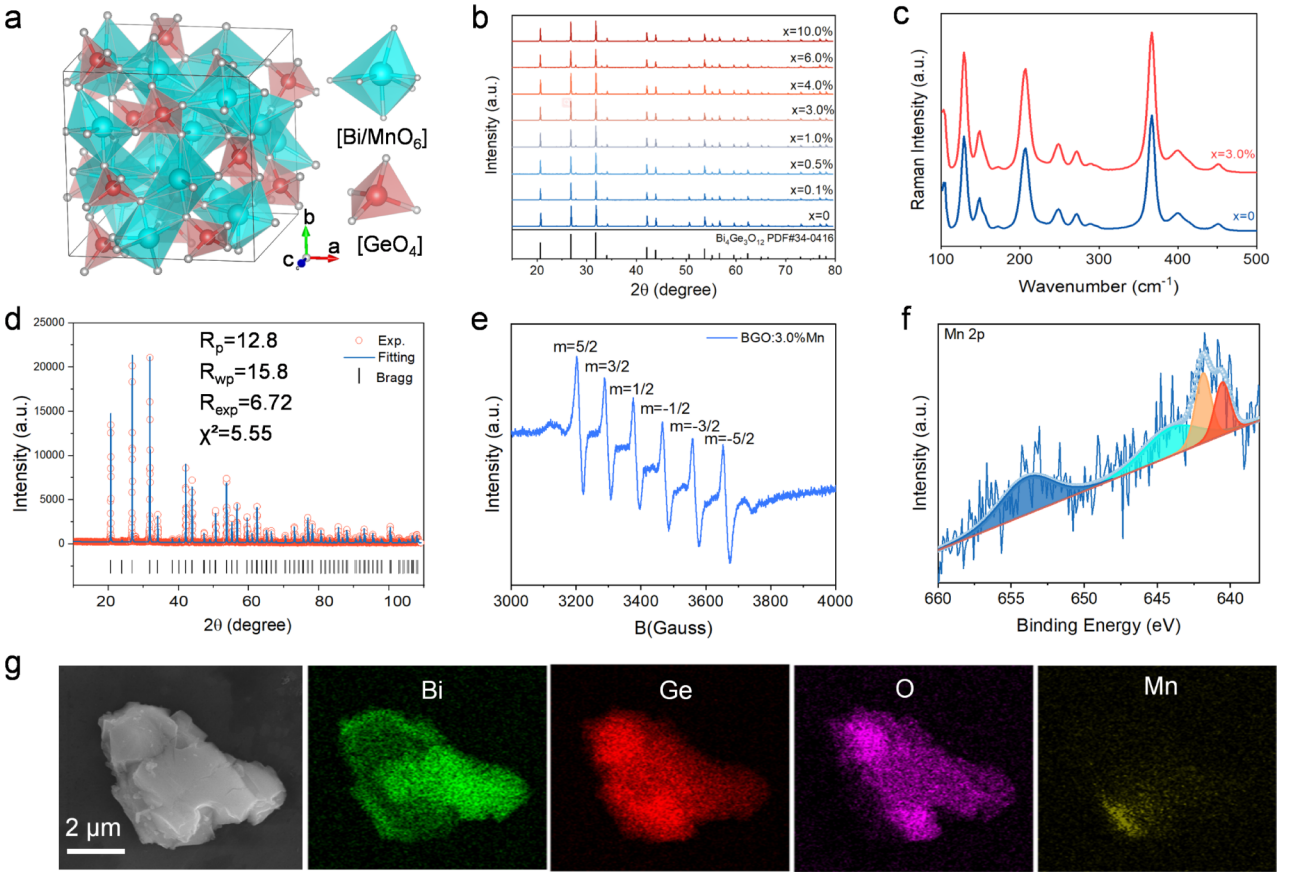

Figure 1. Structural analyses of Mn doping in BGO. (a) Schematic demonstration of crystal structure of BGO and Mn doping sites. (b) XRD patterns of powders with different Mn doping concentrations range from 0 to 10.0%. (c) Raman spectra of BGO and Mn3%. (d) Rietveld refinement of Mn3%. (e) EPR results of Mn3%. (f) XPS curve of Mn 2*p* in Mn10%. (g) EDS mapping of Mn10.0%.

Bi vacancy strategy.[17] It can be seen that most of the existing dopant ions introduce new luminescent centers or afterglows in BGO. Therefore, the rational selection of dopant ions remains challenging.

In this work, we demonstrate that doping Mn^{2+} into BGO can significantly induce improved radiation resistance, and a faster decay time was achieved compared to pure BGO crystals. When the Mn-doped BGO was irradiated continuously for 50 h, more than 80% of its initial luminescence intensity remained. Furthermore, the Mn-doped BGO exhibits a reduction of X-ray excited luminescence intensity to 22%. Additionally, first-principles calculations are combined with advanced tools such as temperature-dependent fluorescence spectroscopy to explore the causes of their radiation resistance enhancement as well as luminescence kinetics studies. These results indicate that Mn-doped BGO materials are promising for applications in HEP experiments. It is expected that this new, robust scintillator will open a window into the field of HEP facilities at the intensity and frontiers.

2. RESULTS AND DISCUSSION

2.1. Structural Analyses of Mn Doping in BGO. The crystal structure of BGO is composed of $[GeO_4]$ tetrahedra and strongly twisted $[BiO_6]$ octahedra,[18] in which Mn replaces Bi to occupy the center of the octahedron, as illustrated in Figure 1a. The X-ray diffraction (XRD) patterns of $Bi_{4-x}Ge_3O_{12}$:*x*Mn with different doping concentrations display similar diffraction peaks, which match well with the PDF cards of pure phase BGO (Figure 1b). There is no obvious displacement of the diffraction peaks after Mn doping, probably due to the fact that the ionic radius of Mn ($R_{Mn^{2+}}$ = 0.83 Å, six-coordinate) is closer to that of Bi ($R_{Bi^{3+}}$ = 1.03 Å, six-coordinate), and a small amount of Mn doping does not cause obvious lattice distortion. This is further confirmed by Raman spectra of pure BGO and Mn3%, as depicted in Figure 1c.

To verify the local crystal environments of Mn^{2+} ions in the lattice, Rietveld refinements were performed for Mn3% (Figure 1d and Table S1), which confirmed the occupation of Mn^{2+} ions at the Bi sites. Electron paramagnetic resonance (EPR) measurements were also conducted. When Mn occupies the Bi site in the lattice, Mn is isolated from each other, and the Mn−Mn interaction is almost negligible. Since Mn is a magnetic nucleus, the EPR spectra show a typical six-peaked hyperfine structure of Mn^{2+} (Figure 1e).

The different oxidation states of Mn ions in powder were detected by X-ray photoelectron spectroscopy (XPS) to deconvolute the Mn 2p spectrum of 10%Mn (Figure 1f). However, the maximum binding energies of Mn^{2+}, Mn^{3+}, and Mn^{4+} overlap.[19] Therefore, in addition to qualitatively determining the Mn^{2+} ion, it is difficult to determine the high energy displacement between Mn^{2+} and Mn^{3+}. The Mn^{2+} oxidation state has a satellite near 640.55 eV due to spin−orbit coupling (MnO), which is not found in the other two oxidation states (Mn^{3+} and Mn^{4+}).[20] Overall, the presence of the satellite qualitatively indicates that manganese exists

https://doi.org/10.1021/acs.cgd.4c01574
Cryst. Growth Des. 2025, 25, 1477−1483

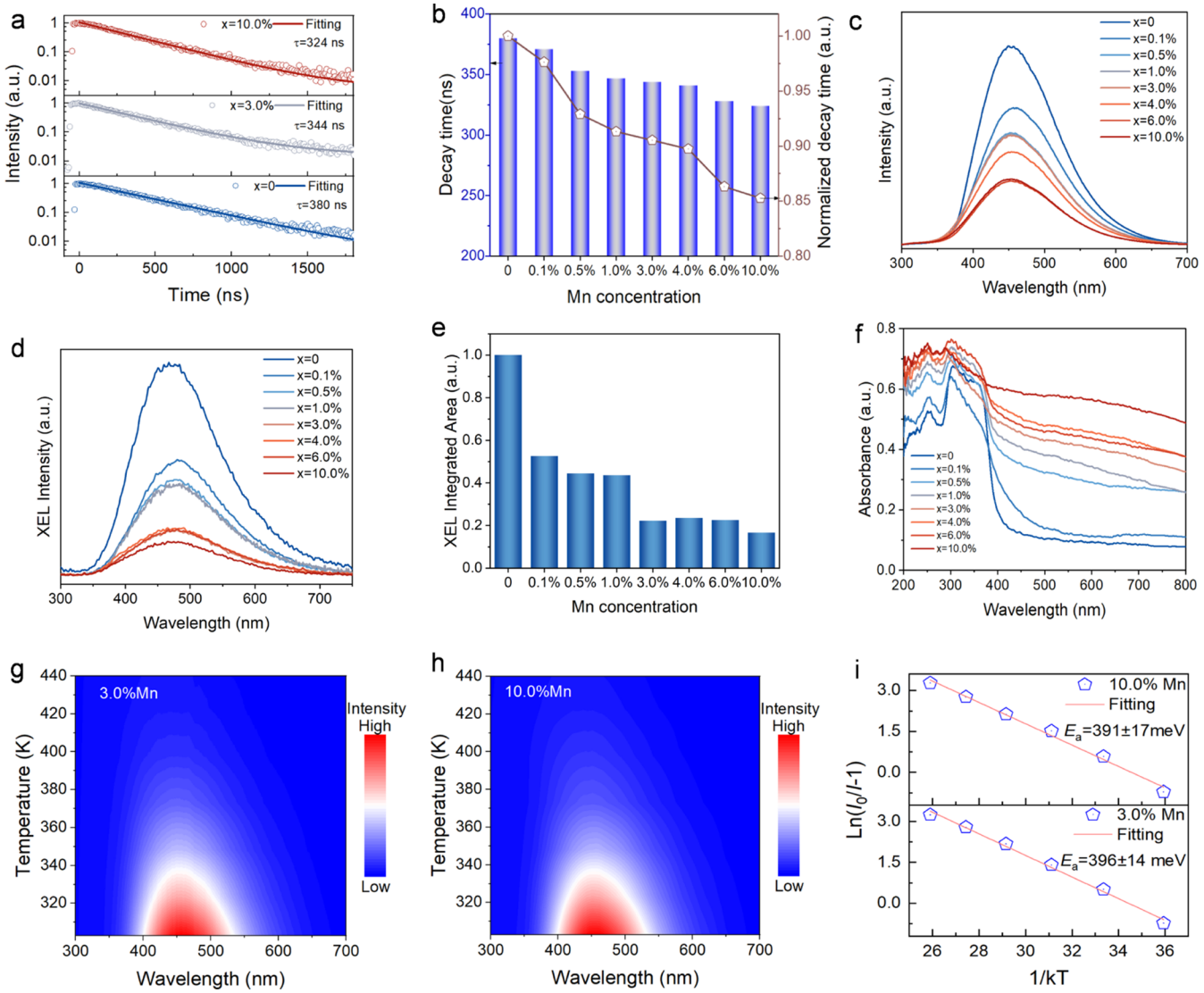

Figure 2. Photoluminescence and scintillation properties of Mn doping in BGO. (a) Decay time curves of pure BGO, Mn0.1%, and Mn3% with an excitation wavelength of 275 nm and a monitor wavelength of 455 nm. (b). Variation of the decay time with the doping concentration. (c) PL spectra of powders with different Mn doping concentrations, from 0 to 10.0%. (d) RL spectra of powders with different Mn doping concentrations from 0 to 10.0%. (e) Variation of integration area of RL intensity with the doping concentration. (f) Absorption spectra with increasing doping concentration. Two-dimensional plots of temperature-dependent PL for (g) Mn3.0% and (h) Mn10%, respectively. (i) $\mathrm{Ln}(I_0/I - 1)$ versus $1/kT$ activation energy graph of Mn3.0% and Mn10.0%. The activation energy (E_a) of the lattice is obtained by fitting the data.

primarily in the form of Mn^{2+} ions. Figures 1g shows the energy dispersive X-ray spectroscopy (EDX) mapping of 10% Mn, where the elements Bi, Ge, and Mn are uniformly distributed in the particles with good homogeneity.

2.2. Photoluminescence and Scintillation Properties. Under the challenge of unprecedentedly high event rates, the fast time response properties of scintillators can significantly reduce signal accumulation, helping to accurately identify signal origins and particle species. Mn doping shortens the fluorescence lifetime from 380 to 344 ns (Mn3.0%) and 324 ns (Mn10.0%), as depicted in Figures 2a and S1. With the increase of doping concentration, the fluorescence lifetime decreases significantly, the fastest shortened to 85% of pure BGO (Figure 2b). It indicates that the shortening of the lifetime was mainly due to the doping effect of Mn.

Photoluminescence spectroscopy helps to identify the origin of luminescence, and it is well-known that the Mn ion is also an important luminescent ion. The excitation spectrum in Figure S2 shows that the doping of Mn did not introduce new excitation peak positions. The photoluminescence spectra in Figure 2c show that the emission in Mn-doped BGO polycrystals is still from the transition of the Bi^{3+} ion $^3P_1 \rightarrow {}^1S_0$. The doping of Mn only changes the luminescence intensity and has little effect on the luminescence peak. This allows BGO:Mn to still be a good match for SiPM. The statistical results of the luminescence peak and integral area in Figure S3 show that Mn doping gradually reduces the luminescence intensity. Doping with Mn3% reduces the photoluminescence intensity and integral area intensity to 57% and 55% of those observed in pure BGO, respectively. When the doping concentration is up to 10%, the photoluminescence intensity is 33% of the original.

RL spectra were conducted to verify their scintillation properties, as illustrated in Figure 2d. With the increase in Mn doping concentration, the RL intensity gradually decreases. When the doping concentration is 3.0%, the integral area is

https://doi.org/10.1021/acs.cgd.4c01574
Cryst. Growth Des. 2025, 25, 1477−1483

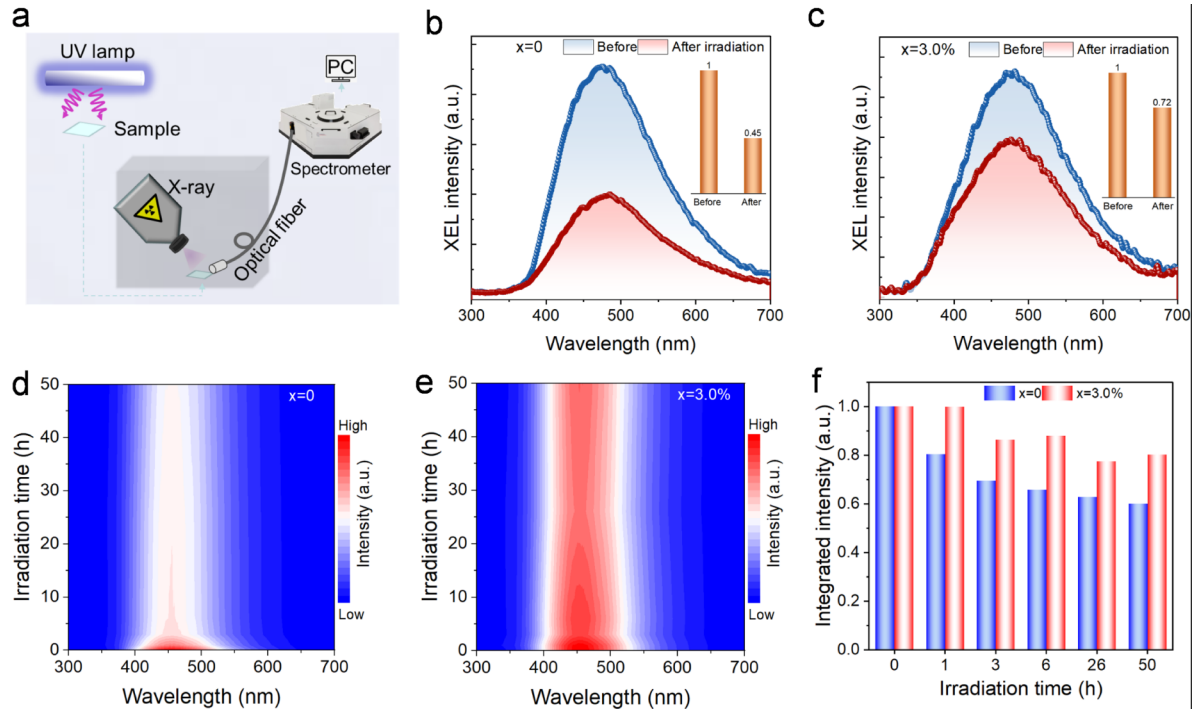

Figure 3. PL and RL results of pure BGO and Mn3.0%-doped BGO powder before and after UV irradiation. (a) Sketch of the device for delivering UV irradiation dose. RL spectra of (b) pure BGO and (c) Mn3.0% before and after UV radiation for 120 min. Two-dimensional plots of irradiation-time-dependent PL for (d) pure BGO and (e) Mn3.0%, respectively. (f) Trend plot of PL integral intensity with the radiation time.

22.3% of pure BGO (Figure 2e). The intensity is basically stabilized when further increased. In addition, RL did not exhibit luminescence from divalent Mn ions, suggesting that Mn ions may act as a trap level in the lattice rather than a luminescence center. The decrease in luminescence intensity may be mainly attributed to the enhanced absorption at the visible wavelength (Figure 2f). The absorption values in the 400−800 nm band gradually increase with increasing doping concentration. As the doping concentration is as high as 10%, the absorption value in the visible part is greater than 50%, and the sample color gradually changes from white powder to gray-black.

Temperature-dependent PL spectrum testing was carried out to gain further insights into the effect of Mn doping on the emission of BGO (Figure 2g,h). The luminescence intensity of both the pure BGO and the low- and high-concentration Mn-doped samples gradually decreases with increasing temperature from 303 to 428 K under excitation at 276 nm, since the nonradiative transition recombination rate of Bi^{3+} ion $^3P_1$-$^1S_0$ increases. Moreover, the luminescence peak is slightly blue-shifted, which may be due to the change of carrier distribution from the $^3P_1$ to $^1S_0$ transition under thermal disturbance.

Based on the Arrhenius plot of the PL intensity versus the reciprocal of temperature (Figure 2i),

$$I(T) = \frac{I_0}{1 + A\exp\left(-\frac{E_a}{kT}\right)}$$

in which $I(T)$ and I_0 represent the PL intensity at the experimental temperature and 303 K. A is a constant, E_a is the activation energy, k represents the Boltzmann constant, and T is the test temperature. The activation energies were determined to be 396 ± 14 and 391 ± 17 meV in 3% and 10% Mn-doped BGO, respectively. Compared with our previously reported activation energy for pure BGO (382 meV), Mn doping slightly increases the thermal activation energy, which is still slightly lower than that of Ce doping.[17] The enhanced thermal stability of BGO:Mn reflects that introducing Mn hinders the energy transfer from the excited state to nonradiative transition centers.[21]

2.3. Radiation Resistance Ability. Radiation resistance is another key indicator for evaluating the performance of scintillation materials because all materials are inevitably suffered from radiation damage, especially for future HEP calorimeters operating under unprecedented luminosity.[4,12,22] For scintillation crystals, the physical mechanism of radiation damage is mainly the result of the combined effect of the micro/macro defect structures present in the crystal and the color centers caused by irradiation.

Although the radiation resistance of scintillators is mainly under gamma-ray source exposure, gamma irradiation sources often require specialized radiation environments, and the testing process is complicated, time-consuming, and extremely costly. Using ultraviolet light (UV) as the radiation source is a method to evaluate the radiation resistance of scintillators Figure 3a is a sketch of the device used to evaluate the radiation resistance of powder scintillation samples. First, the powder sample is irradiated under a UV lamp for different times, and then, the RL spectrum of the sample is immediately tested under X-ray excitation. After high-power UVB radiation for 120 min, the RL intensity of the pure BGO samples decreased significantly, but the peak position of the luminescence was not shifted (Figure 3b). The inset shows that the RL integrated intensity is reduced to 45% of the initial one. The Mn3.0% sample still has 72% of the initial integrated intensity after 120 min of UV irradiation, showing excellent resistance to radiation (Figure 3c). In addition to testing the RL after high-power UV radiation, the PL spectra were also

https://doi.org/10.1021/acs.cgd.4c01574
Cryst. Growth Des. 2025, 25, 1477−1483

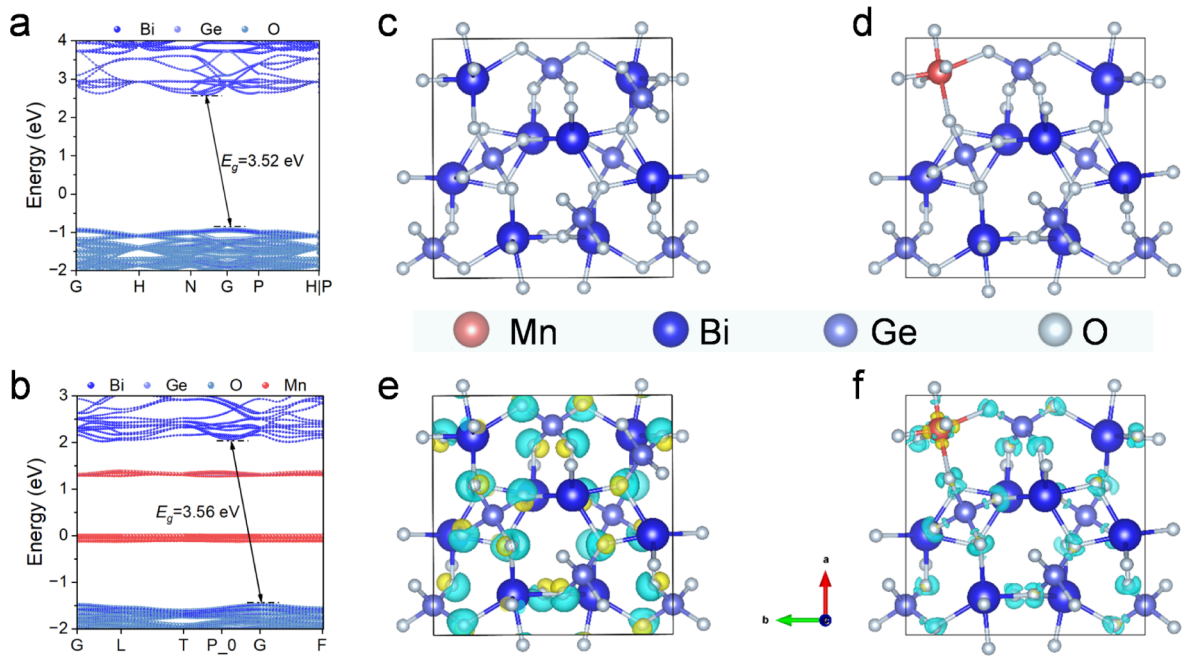

Figure 4. DFT calculations of Mn doping in BGO. (a,b) Fat-band structure, (c,d) crystal structure, and (e,f) charge density difference of BGO and Mn doping BGO. In panels (e) and (f), cyan represents depletion of electrons and yellow represents accumulation of electrons. The isosurface level is 0.03.

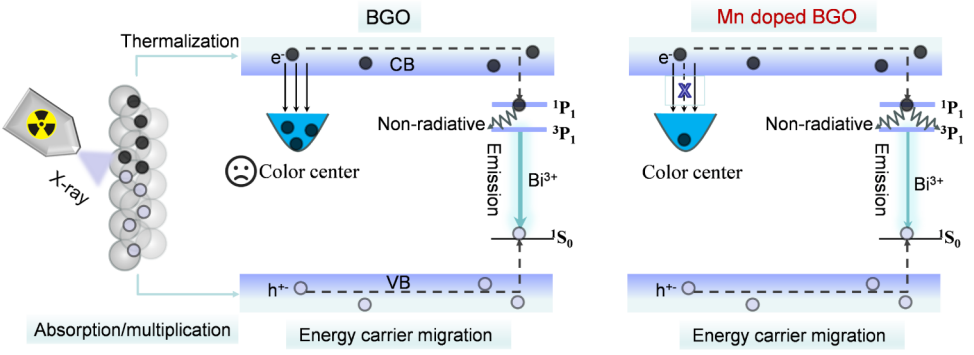

Figure 5. Proposed RL modulation mechanism in Mn-doped BGO.

tested after irradiation for different times (Figures 3d,e). Similarly, radiation damage did not cause a shift in the PL peak position. The Mn-doped samples showed much less radiation damage. After 50 h of UV irradiation, the luminescence integral intensity remained at about 80% of the initial one, while for the pure BGO, it was 60% of the initial one. This is consistent with the results shown by RL.

2.4. Theoretical Calculations. Theoretical calculations were carried out to evaluate the effect of Mn doping in the BGO crystal. Figure 4a,b shows the fat-band structures of pure BGO and Mn-doped BGO. The pure BGO has a wide forbidden bandwidth of about 3.52 eV, which is consistent with the previous study.[17,23] Such a wide band gap creates a good host condition for the introduction of Mn doping.[24] The top of its valence band is mainly coupled by the 2p electron orbitals of the the valence band of the O group, and the bottom of the conduction band consists of the 5d electron orbitals of Bi. Additionally, the Mn doping introduces additional energy levels, and the difference between the two impurity energy levels is about 1.3 eV. According to the fat-band diagram, these levels mainly originate from the orbitals of Mn. These deep energy levels can initiate the capture of carriers and energy storage mechanisms in the scintillator. This may be the reason Mn doping induces a decrease in scintillation luminescence, as well as an increase in radiation resistance.

To gain insight into the effect of the doping effect of Mn on the local electronic structure, pure and Mn-doped crystal structures of BGO were constructed (Figure 4c,d). Radiation resistance decreasing in the oxide scintillator is thought to originate from the oxygen deficiency color center, which forms a color center by trapping electrons.[25] Differential charge density plots show that there is the accumulation and transfer depletion of electrons mainly centered around O atoms in pure BGO (Figure 4e). This may be the main reason that the radiation resistance of pure BGO is not prominent enough. In contrast, the depletion of electrons around O is greatly weakened after Mn doping, and the accumulation of electrons disappears (Figure 4f). Unexpectedly, the electrons show accumulation at the Mn atomic positions. This suggests that Mn doping creates intermediate energy levels in the forbidden band to capture carriers, weakening the ability of oxygen-

https://doi.org/10.1021/acs.cgd.4c01574
Cryst. Growth Des. 2025, 25, 1477−1483

deficient capture of electrons to form color centers.[26,27] This greatly improves the radiation resistance of the Mn-doped BGO crystals.

2.5. Modulation Mechanism of Mn Doping in BGO. We propose a possible mechanism for Mn doping to enhance the scintillation performance, especially the enhanced radiation resistance and fastened decay kinetics, as shown in Figure 5. Scintillation is a complex process that can usually be simplified into three consecutive processes.[28] (1) Absorption/multiplication: The absorption of a high-energy particle will produce an inner shell hole and a primary electron. The multiplication of electrons and holes occurs through secondary X-rays, the Auger process, and inelastic electron/electron scattering. When the electron energy is less than the ionization threshold, the electrons and holes are thermalized to the conduction band and the valence band, respectively. Electrons and holes can remain free or combine to form free or self-trapped excitons. (2) Energy carrier migration: energy carriers are transferred to the luminous center. In this process, pure BGO with oxygen deficiency will capture electrons forming color centers, which is detrimental to the crystal's ability to withstand high-energy radiation. (3) Emission: excited electrons recombine with holes to release energy by emitting photons, accompanied by a nonradiative relaxation process. Mn doping introduces new impurity energy levels in the forbidden band, which inhibits the formation of color centers from oxygen deficiency by capturing electrons, thus greatly improving the radiation resistance (Figure 4). Moreover, Mn doping induces an increase in the nonradiative relaxation probability, which results in a decrease in luminescence intensity accompanied by a faster decay time. This is precisely the same reduction in light output and a faster decay time required for HEP applications.

3. CONCLUSIONS

In summary, this work presents a new Mn-doped BGO powder with an exceptionally faster decay time and enhanced radiation resistance. Mn doping not only does not change the intrinsic luminescence peak of BGO but also introduces a new intermediate energy level in the energy band to inhibit the formation of color centers. The fluorescence lifetime was gradually shortened with an increasing Mn doping concentration. Mn10.0% ion doping resulted in a 15% acceleration of the fluorescence lifetime from 380 to 324 ns. When the doping concentration was 3.0%, the PL intensity and RL intensity decreased to 55% and 22% of those of pure BGO, respectively. The stronger scintillation luminescence intensity reduction is mainly due to the nonradiative transition control. Mn doping also imparts strong radiation resistance, and the 3% Mn-doped sample still has 72% of the initial RL integrated intensity after 2 h of UV radiation, which is better than that of the pure sample (45%). After 50 h of UV radiation, the fluorescence luminescence integral intensity of the Mn-doped sample remained at about 80% of the initial one. Future work should be directed toward the growth of high-quality and performance-optimized BGO crystals with Mn doping. This work also provides an idea for searching for or rediscovering novel scintillators from existing classic, cost-effective scintillators for high-energy physics.

4. EXPERIMENTAL METHODS

4.1. Computational Methods. First-principles calculations were performed on the basis of density functional theory (DFT) via the Vienna ab initio simulation package (VASP) code,[29,30] and the generalized gradient approximation (GGA) by the Perdew–Burke–Ernzerhof (PBE) formulation was used. The plane-wave cutoff energy was 400 eV, and the Brillouin zone integral was set to a 2 × 2 × 2 Monkhorst–Pack grid with a *K*-point sampling scheme. The stopping criterion for the ionic optimization number and the total energy allowed error criterion are −0.03 $Å^{-1}$ and 1.0×10^{-6} eV, respectively. In the Mn-BGO structural model, one Mn atom was applied to substitute one of the Bi atoms in one conventional cell of $Bi_4Ge_3O_{12}$, whose stoichiometry is $Bi_{28}Ge_{21}O_{84}$.

4.2. Materials Preparation. A series of $Bi_{4-x}Ge_3O_{12}$:Mn (x = 0–10%) samples were prepared via the high-temperature solid-phase method. Stoichiometric amounts of the starting materials, Bi_2O_3 (4N), GeO_2 (4N), and $MnCO_3$ (4N), were mixed thoroughly in an agate mortar by grinding and sintered at 900 °C for 6 h in air. The sample was cooled to room temperature for subsequent characterization.

4.3. Materials Characterizations. The as-prepared powder samples were carried out on a Bruker D8 ADVANCE X-ray diffractometer using Cu Kα (λ = 1.5418 Å) radiation. Raman spectra were tested on an HR Evolution (HORIBA, France) with the excitation of a 532 nm laser. EPR was carried out on the EMXnano of Bruker. XPS measurements were performed on an Axis Ultra of Kratos Analytical-A (Shimadzu Group company) with an Al (Mono) source (75 W). SEM and TEM were characterized by a Magellan 400 field emission scanning electron microscope from American FEI Company Corporation and a JEM-2100F field emission electron microscope from Japan JEOL Co., Ltd. Photoluminescence (PL) and PL excitation (PLE) spectra were tested on a Hitachi F-4600 fluorescence spectrophotometer with a 150 W xenon arc lamp as the light source. The UV–visible absorption spectrum was measured with a UV-3600 spectrophotometer (Shimadzu, Japan) ranging from 200 to 800 nm, and $BaSO_4$ is the reflectance sample. The in situ temperature-dependent PL spectra (303 K–428 K) were measured on a Hitachi F-4600 with TAP-02 high-temperature fluorescence test accessories. RL was measured with Edinburgh Instruments FLS920.

■ ASSOCIATED CONTENT

Data Availability Statement

The data supporting this article have been included as part of the Supporting Information. More raw data are available from the corresponding author upon reasonable request.

Supporting Information

The Supporting Information is available free of charge at https://pubs.acs.org/doi/10.1021/acs.cgd.4c01574.

Decay time curves, excitation spectra, PL integrated area, and X-ray structure refinement parameters (PDF)

■ AUTHOR INFORMATION

Corresponding Authors

Mingxue Deng – *Shanghai Institute of Ceramics, Chinese Academy of Sciences, Shanghai 201899, China*; Email: dengmingxue@mail.sic.ac.cn

Junfeng Chen – *Shanghai Institute of Ceramics, Chinese Academy of Sciences, Shanghai 201899, China*; orcid.org/0000-0003-3863-3324; Email: jfchen@mail.sic.ac.cn

Authors

Lei Chen – *Shanghai Institute of Ceramics, Chinese Academy of Sciences, Shanghai 201899, China*

Xiang Li – *Shanghai Institute of Ceramics, Chinese Academy of Sciences, Shanghai 201899, China*

Xuejun Qi – *Shanghai Institute of Ceramics, Chinese Academy of Sciences, Shanghai 201899, China*

Shaohan Wang – *Shanghai Institute of Ceramics, Chinese Academy of Sciences, Shanghai 201899, China*

https://doi.org/10.1021/acs.cgd.4c01574
Cryst. Growth Des. 2025, 25, 1477–1483

Complete contact information is available at:
https://pubs.acs.org/10.1021/acs.cgd.4c01574

Author Contributions

M.D.: conceptualization, data curation, formal analysis, investigation, methodology, and writing—original draft; L.C.: data curation; X.L.: data curation; X.Q.: investigation; S.W.: data curation; J.C.: conceptualization, funding acquisition, project administration, resources, supervision, and writing—review and editing.

Notes

The authors declare no competing financial interest.

■ ACKNOWLEDGMENTS

Junfeng Chen would like to acknowledge the National Key Technologies R&D Program of China (grant number: 2023YFA1606300) and the Strategic Priority Research Program of the Chinese Academy of Sciences (grant number: XDA25030600). Mingxue Deng would like to thank the support by the State Key Laboratory of Particle Detection and Electronics, SKLPDE-KF-202402.

■ REFERENCES

(1) Conroy, G. China could start building world's biggest particle collider in 2027. *Nature* **2024**, *630*, 801−802.
(2) Gao, J. CEPC Technical Design Report: Accelerator. *Radiation Detection Technology And Methods* **2024**, *8* (1), 1−1105.
(3) Liu, Y.; Jiang, J.; Wang, Y. High-granularity crystal calorimetry: conceptual designs and first studies. *J. Instrum.* **2020**, *15* (4), C04056.
(4) Zhu, R.-Y. Ultrafast and Radiation Hard Inorganic Scintillators for Future HEP Experiments. *J. Phys.: Conf. Ser.* **2019**, *1162* (1), 012022.
(5) Qi, B.; Liu, Y. R&D of a Novel High Granularity Crystal Electromagnetic Calorimeter. *Instruments* **2022**, *6* (3), 40.
(6) Acerbi, F.; Gundacker, S. Understanding and simulating SiPMs. *Nucl. Instrum. Methods Phys. Res., Sect. A* **2019**, *926*, 16−35.
(7) Adeva, B.; Aguilar-Benitez, M.; Akbari, H.; Alcaraz, J.; Aloisio, A.; Alvarez-Taviel, J.; Alverson, G.; Alviggi, M. G.; Anderhub, H.; Anderson, A. L.; et al. The construction of the L3 experiment. *Nucl. Instrum. Methods Phys. Res., Sect. A* **1990**, *289* (1), 35−102.
(8) Zhang, L.; He, J.; deBoer, R. J.; Wiescher, M.; Heger, A.; Kahl, D.; Su, J.; Odell, D.; Chen, Y.; Li, X.; et al. Measurement of $^{19}F(p,\gamma)^{20}Ne$ reaction suggests CNO breakout in first stars. *Nature* **2022**, *610* (7933), 656−660.
(9) Spurrier, M. A.; Szupryczynski, P.; Yang, K.; Carey, A. A.; Melcher, C. L. Effects of Ca^{2+} Co-Doping on the Scintillation Properties of LSO: Ce. *IEEE Trans. Nucl. Sci.* **2008**, *55* (3), 1178−1182.
(10) Chen, J.; Yang, F.; Zhang, L.; Zhu, R. Y.; Du, Y.; Wang, S.; Sun, S.; Li, X. Slow Scintillation Suppression in Yttrium Doped BaF_2 Crystals. *IEEE Trans. Nucl. Sci.* **2018**, *65* (8), 2147−2151.
(11) Peng, C.; Zhang, K.; Yang, L.; Zheng, J.; Lu, Y.; Hou, Y.; Yan, X.; Shi, Z.; Han, H.; Song, Z.; et al. Investigation on the Fast Component Light Yield of BaF_2: Y Crystal. *IEEE Trans. Nucl. Sci.* **2022**, *69* (9), 2083−2088.
(12) Li, X.; Chen, J.; Yang, D.; Chen, X.; Geng, D.; Jiang, L.; Wu, Y.; Meng, C.; Zeng, H. Mn^{2+} induced significant improvement and robust stability of radioluminescence in $Cs_3Cu_2I_5$ for high-performance nuclear battery. *Nat. Commun.* **2021**, *12* (1), 3879.
(13) Wei, Z. Y.; Zhu, R. Y.; Newman, H.; Yin, Z. W. Radiation resistance and fluorescence of europium doped BGO crystals. *Nucl. Instrum. Methods Phys. Res., Sect. A* **1990**, *297* (1-2), 163−168.
(14) Belman-Rodriguez, C.; Ponce-Perez, R.; Reyes, A. M.; Galindez-Jamioy, C. A.; Soto, G.; Farías, M. H.; Guerrero-Sánchez, J.; Moreno-Armenta, M. G.; Reyes-Serrato, A.; Aguila, S. A. Experimental and theoretical assessment of the Eu^{3+} doped $Bi_4Ge_3O_{12}$. *J. Alloys Compd.* **2023**, *966*, 171567.
(15) Okazaki, K.; Fukushima, H.; Nakauchi, D.; Okada, G.; Onoda, D.; Kato, T.; Kawaguchi, N.; Yanagida, T. Investigation of Er: $Bi_4Ge_3O_{12}$ single crystals emitting near-infrared luminescence for scintillation detectors. *J. Alloys Compd.* **2022**, *903*, 163834.
(16) Dunaeva, E. E.; Ivleva, L. I.; Doroshenko, M. E.; Boldyrev, K. N.; Papashvili, A. G. Growth and spectral-luminescence characteristics of modified BGO crystals. *J. Cryst. Growth* **2019**, *525*, 125205.
(17) Deng, M.; Tang, Y.; Chen, J.; Tang, Y.; Wang, J.; Sun, T.; Wang, M.; Zhu, J.; Zhou, Z.; Wang, J. Bismuth Vacancy-Induced Enhancement of Luminescence Intensity and Irradiation Resistance for $Bi_4Ge_3O_{12}$. *J. Phys. Chem. Lett.* **2023**, *14* (16), 3818−3825.
(18) Bravo, D.; López, F. J. An electron paramagnetic resonance study of Er^{3+} in $Bi_4Ge_3O_{12}$ single crystals. *J. Chem. Phys.* **1993**, *99* (7), 4952−4959.
(19) Su, B.; Zhou, G.; Huang, J.; Song, E.; Nag, A.; Xia, Z. Mn2+-Doped Metal Halide Perovskites: Structure, Photoluminescence, and Application. *Laser Photonics Rev.* **2021**, *15* (1), 2000334.
(20) Zhou, X.; Han, K.; Wang, Y.; Jin, J.; Jiang, S.; Zhang, Q.; Xia, Z. Energy-Trapping Management in X-Ray Storage Phosphors for Flexible 3D Imaging. *Adv. Mater.* **2023**, *35* (16), 2212022.
(21) Tang, Y.; Deng, M.; Liu, Q.; Kang, C.; Li, X.; Zheng, J.; Suenaga, K.; Zhou, Z.; Chen, J.; Wang, J.; Liu, Q. Reducing Luminescence Intensity and Suppressing Irradiation-induced Darkening of $Bi_4Ge_3O_{12}$ by Ce-doping for Radiation Detection. *Adv. Opt. Mater.* **2024**, *12* (2), 2301332.
(22) Zaffalon, M. L.; Cova, F.; Liu, M.; Cemmi, A.; Di Sarcina, I.; Rossi, F.; Carulli, F.; Erroi, A.; Rodà, C.; Perego, J.; et al. Extreme γ-ray radiation hardness and high scintillation yield in perovskite nanocrystals. *Nat. Photonics* **2022**, *16* (12), 860−868.
(23) Akande, S. O.; Bouhali, O. First-principles studies of defect behaviour in bismuth germanate. *Sci. Rep.* **2022**, *12* (1), 15728.
(24) Deng, M.; Liu, Q.; Zhang, Y.; Wang, C.; Guo, X.; Zhou, Z.; Xu, X. Novel Co-Doped Y_2GeO_5: Pr^{3+},Tb^{3+}: Deep Trap Level Formation and Analog Binary Optical Storage with Submicron Information Points. *Adv. Opt. Mater.* **2021**, *9* (10), 2002090.
(25) Zhu, R. Y.; Deng, Q.; Newman, H.; Woody, C. L.; Kierstead, J. A.; Stoll, S. P. A study on the radiation hardness of lead tungstate crystals. *IEEE Trans. Nucl. Sci.* **1998**, *45* (3), 686−691.
(26) Han, K.; Jin, J.; Wang, Y.; Zhou, X.; Sun, Y.; Chen, L.; Xia, Z. Hybrid Eu(II)-bromide scintillators with efficient 5d-4f bandgap transition for X-ray imaging. *Light: Sci. Appl.* **2024**, *13* (1), 222.
(27) Jin, J.; Han, K.; Wang, Y.; Xia, Z. Bandgap Narrowing in Europium(II)-Based Bromide Hybrids toward Improved X-ray Scintillation and Imaging. *Chem. Mater.* **2024**, *36* (9), 4813−4820.
(28) Bizarri, G. Scintillation mechanisms of inorganic materials: From crystal characteristics to scintillation properties. *J. Cryst. Growth* **2010**, *312* (8), 1213−1215.
(29) Kresse, G.; Furthmüller, J. Efficiency of ab-initio total energy calculations for metals and semiconductors using a plane-wave basis set. *Comput. Mater. Sci.* **1996**, *6* (1), 15−50.
(30) Matsuzawa, T.; Aoki, Y.; Takeuchi, N.; Murayama, Y. A New Long Phosphorescent Phosphor with High Brightness, $SrAl_2O_4$: Eu^{2+},Dy^{3+}. *J. Electrochem. Soc.* **1996**, *143* (8), 2670−2673.